JOURNAL OF THE AMERICAN CHEMICAL SOCIETY
ARTICLE
pubs.acs.org/JACS

Crystalline Hydration Structure at the Membrane–Fluid Interface of Model Lipid Rafts Indicates a Highly Reactive Boundary Region

Khizar H. Sheikh* and Suzanne P. Jarvis

Nanoscale Function Group, Conway Institute of Biomolecular and Biomedical Research, University College Dublin, Belfield, Dublin 4, Ireland.

Supporting Information

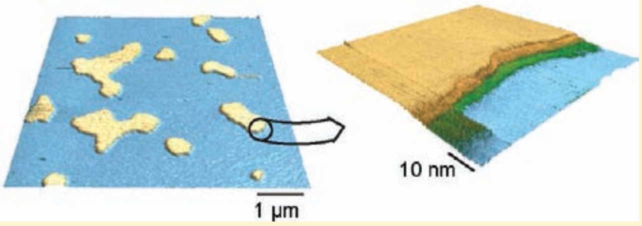

ABSTRACT: The fluid mosaic model of biological membranes is that of a two-dimensional lipid bilayer in which both lipids and associated membrane proteins diffuse freely. More recently, the raft hypothesis proposed that membranes contain small, dynamic, functional domains (rafts), which act as platforms for membrane protein attachment and interaction. Although experimental evidence supporting the raft hypothesis is growing, very little is known of the structure of the membrane–fluid interface of lipid raft systems. Here, we report the direct submolecular-scale imaging of model raft membranes using ultrahigh resolution atomic force microscopy. We characterize the heterogeneous nature of crystalline hydration layers at the membrane–fluid interface. The association of crystalline hydration layers with raft membranes would significantly affect the mechanism and kinetics of both inter-raft interactions and those between rafts and external biomolecules, and therefore this finding has important implications for membrane biology.

INTRODUCTION

The raft hypothesis proposes that the cell membrane contains small (<200 nm) dynamic functional domains, enriched in sphingolipids and cholesterol and associated with specific types of membrane proteins.[1] The hypothesis arose from the discovery that the apical surfaces of the plasma membranes of epithelial cells contained fractions exhibiting resistance to solubilization by the detergent Triton X-100.[1] These detergent-resistant membranes (DRMs), which were also found to exist in other types of cells, were found to be enriched in sphingolipids and cholesterol.[2−4] The raft concept of membrane compartmentalization has profound implications for membrane functions such as cell signaling, intracellular lipid and protein trafficking, and viral and toxin interactions. Certain types of membrane proteins have been found to preferentially associate with DRMs, and both rafts and raft-associated proteins have been found to be targets for a wide range of diseases.[5]

Experimental evidence supporting the raft hypothesis is growing, based on indirect imaging techniques such as single particle and single fluorophore tracking,[6−8] fluorescence energy resonance transfer,[9] and electron spin resonance,[10] as well as by direct imaging techniques such as amplitude modulation atomic force microscopy (AM-AFM)[11] and electron microscopy (EM).[2] The resolution of these available tools greatly limits the structural study of such small, dynamic structures, and therefore many questions remain regarding the size, structure, formation, regulation, and lifetime of rafts.[12]

AM-AFM has been used in imaging studies of cellular membranes and solid supported planar membranes for over a decade.[13,14] With subnanometer scale height resolution, height differences arising from differing acyl chain packing between raft and nonraft domains can readily be detected. Unlike EM, AFM has the ability to image membranes in aqueous physiological buffers, an ability that is particularly advantageous. The AFM tip can also be used to probe the surface to elucidate the hydration and mechanical properties of the surface.[15,16] Significant improvements in lateral resolution have occurred in recent years, with atomic resolution of the chemical structure of an individual molecule recently being achieved using frequency modulation AFM (FM-AFM) in a UHV environment at low (5 K) temperatures.[17] Previously in this group, we developed an ultralow deflection noise AFM operating in FM mode.[18] The sensitivity of this instrument affords the capability of imaging surfaces with atomic resolution in fluid environments at room temperature.[19,20] We previously employed this instrument to image short-range ordering and hydration of the lipid headgroups of mica-supported dipalmitoylphosphatidylcholine (DPPC) bilayers in phosphate buffer, and more recently imaged mesoscale lipid headgroup ordering in supported DPPC bilayers.[19,21]

In this study, we applied this imaging capability to elucidate the molecular structure and hydration of a widely used three-component model raft membrane system composed of sphingomyelin (SM), cholesterol and an unsaturated lipid (DOPC). Photophysical studies mapping the phase behavior of model raft membranes show the phase separation of these mixtures into SM/cholesterol-rich domains (model rafts) and phosphatidylcholine-rich/cholesterol-poor domains at temperatures comparable

Received: July 21, 2011
Published: October 11, 2011

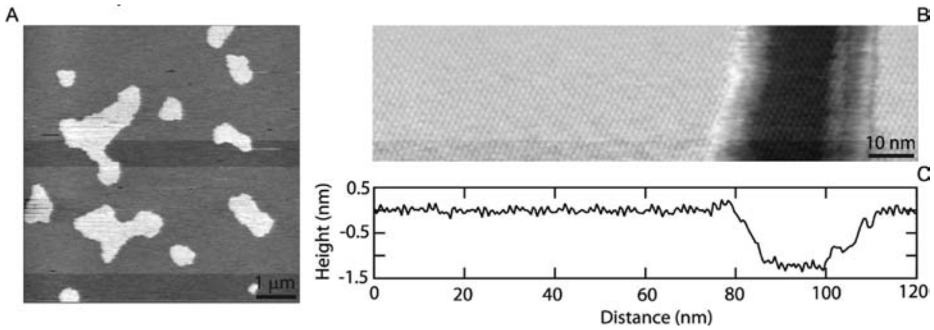

Figure 1. (A) Micrometer-scale AM-AFM height image of the surface of a model lipid raft bilayer composed of a 1:1:1 SM/cholesterol/DOPC mixture imaged in PBS solution at pH 7.4 showing micrometer-scale phase separation of SM/cholesterol-rich raft domains (lighter regions) and DOPC-rich nonraft domains (darker background), tip velocity 28.9 μm/s, *z*-scale 2 nm (*black* to *white*), pixel width 27.3 nm. (B) High-resolution FM-AFM height image of a model raft surface imaged in PBS solution at pH 7.4 showing mesoscale orthorhombic ordering of the headgroups of the lipid molecules forming the raft domain. Lipid headgroup ordering of nonraft phase by the two raft domain boundaries can also be seen, tip velocity 584 nm/s, *z*-scale 2 nm (*black* to *white*), pixel width 4.7 Å. (C) Cross section of height image (B).

to DRM studies.[22] Studies of model raft membranes have shown the SM/cholesterol-rich phase to exhibit resistance to solubilization by nonionic detergents such as Triton X-100.[23] This has led to the association of DRMs with model membrane SM/cholesterol-rich domains. However, the model rafts represent a significantly less complex system as they do not contain the full complement of cellular membrane proteins or the wide range of lipid species seen in vivo. Additionally, unlike in vivo rafts, the model membrane raft system used in this study is supported on a mica substrate and will be in thermodynamic equilibrium. We should note that in subsequently using the term raft, we are referring to the model raft system, unless otherwise stated.

Here, we image, with submolecular resolution, the crystalline molecular order of lipids forming model raft domains as well as the induced molecular ordering of the nonraft phase immediately surrounding raft domains. We also detected the presence of hydration layers at the membrane–fluid interface using force probing with the AFM tip and directly imaged their crystalline structure with ångstrom resolution. We detected a thin intermediate bilayer between the raft and nonraft phases which did not have detectable hydration layers. We also imaged crystalline hydration layers associated with the nonraft phase immediately surrounding the rafts where molecular ordering had been induced. We discuss the implications of the existence and structure of crystalline hydration layers on the interaction of rafts with membrane proteins and external biomolecules.

RESULTS AND DISCUSSION

Micrometer-Scale Imaging of Model Raft Domains. All samples analyzed were prepared using equimolar mixtures of palmitoylsphingomyelin (SM), di-oleoylphosphatidylcholine (DOPC), and cholesterol. Phase diagrams from photophysical studies of SM/phosphatidylcholine/cholesterol mixtures at room temperature show the components to be in a two-phase co-existence regime. The raft phase is composed predominantly of SM and cholesterol, and the nonraft phase, predominantly of DOPC. Figure 1A shows a 7 μm square AFM image of the model bilayer, formed on a mica substrate in phosphate-buffered saline (PBS) buffer at pH 7.4, obtained in AM imaging mode.

The SM/cholesterol-rich raft domains can be seen as the higher (lighter) domains in a background fluid DOPC/cholesterol nonraft phase. The height difference between the two phases is 0.8 ± 0.1 nm and arises from a difference in the acyl chain conformation between the raft phase, where the saturated SM acyl chains are in a more extended (trans) conformation compared to the nonraft phase where the unsaturated DOPC acyl chains contain cis double bonds. The measured height differences are in good agreement with previous measurements,[14,23] but it should be noted that bilayer height measurements are dependent on both tip imaging force and geometry, and therefore direct comparisons between different studies may not be always be valid.[16] The diameters of the model raft domains varied considerably, both within sample and sample to sample, but were typically in the 500–3000 nm range. The domain sizes are in agreement with previous measurements, given the difference in bilayer formation times, and we note that domain nucleation and growth are highly dependent on the thermal history of the sample.[23,24] The shape of the domain edges provides us with clues as to the phase state of the model raft domains. Both rounded and straight edges can be seen at the model raft boundary edges. This would suggest that the model raft domains are in a pseudocrystalline phase.

Nanometer-Scale Imaging of Model Raft Domains. Figure 1B shows a 120 nm by 30 nm image taken at the edges of two neighboring model raft domains, taken in FM imaging mode with an imaging force of ~15 pN, about an order of magnitude less than that used for AM imaging. The height difference between the raft and nonraft domains as shown by the height cross section in Figure 1C is 1.2 ± 0.1 nm. It should be noted that the different tip imaging force between AM and FM measurements will significantly affect the AFM height measurement of the lipid bilayers.[16]

Ordered protrusions corresponding to the lipid headgroup moieties are clearly visible in the raft phase. The diameter of these protrusions is 2.7 ± 0.5 Å (fwhm) with heights of 1.25 ± 0.25 Å. The separation of the protrusions is 5.3 ± 0.5 Å (along an axis running diagonally from lower-right to upper-left of the image) and 4.5 ± 0.5 Å (along an axis running from upper-right to lower-left of the image), with an angle of 62 ± 5° between the axes.

It should be noted that the size of the protrusions will be convoluted by the AFM tip radius. The AFM tip is composed of silicon, and the terminal atoms at the apex of the tip will possess dangling bonds that will oxidize in aqueous solution to terminate in either silanol or siloxane groups. The magnitude of the van der Waals radii of hydrogen, oxygen, and silicon are 1.09, 1.52, and 2.10 Å, respectively.[25] When compared to the observed diameter of the protrusions, we surmise that the apex of the AFM tip was atomically sharp. When compared with the observed protrusion heights, we conclude that the AFM tip apex does not penetrate the headgroup structure by more than a single atomic diameter, sterically limited by the separation of the headgroups in relation to the tip radius. The effect of this steric hindrance will be to reduce the apparent diameter of the protrusions, but not the periodicity of the protrusions.

The size and separation of the protrusions are consistent with their assignment to that of the phosphate and choline moieties of the lipid headgroups. This assignment is in agreement with neutron diffraction studies,[26] atomistic models,[27] and previous FM-AFM imaging of DPPC bilayers,[19,21] showing that the choline headgroups are oriented roughly parallel to the plane of the bilayer forming an array of surface electric dipoles. Due to the high variation of the mean lateral diameters of the headgroup moieties (in comparison to their magnitude), it was not topographically possible to assign individual protrusions specifically to either a phosphate or choline group. However, previous theoretical modeling of phosphatidylcholine headgroup organization suggests that the surface electric dipoles align in rows, nose-to-tail, and that the polarity of the rows alternates between adjacent rows.[28] The lattice vectors allow the calculation of an average area per molecule of 42 ± 10 Å.^{2} This value is in good agreement with those determined from surface pressure isotherms of sphingomyelin/cholesterol monolayers,[29] although it should be noted that the raft phase will also contain a proportion of DOPC molecules.[22] The area per molecule value also reflects the "condensing effect" of cholesterol on SM (and DOPC) bilayers, although our imaging was unable to directly ascertain the existence of SM/cholesterol complexes, as the AFM tip only profiles the bilayer headgroup region by ~150 pm and (apart from its hydroxyl group) the bulk of the cholesterol molecule lies below the headgroup region.

Of note is that the image shows mesoscale ordering (over a lateral range of at least 80 nm) of the lipid headgroups. The existence of positional ordering over the mesoscale demonstrates that the mica-supported raft domains are in a pseudocrystalline phase state at the imaging temperature (23 ± 1 °C) which is consistent with the straight edged domain morphology previously shown (Figure 1a).

Mesoscale lipid headgroup ordering has previously been observed in mica-supported DPPC bilayers in FM-AFM studies undertaken by this group at temperatures below the main-chain melting transition (T_m).[19,21] Mesoscale crystalline order has also been observed in a wide-angle X-ray diffraction study of fully hydrated unoriented multilamellar DPPC vesicles below $T_{m.}$[30] The crystalline−gel phase transition, observed in DPPC bilayers between 19 and 23 °C below T_m is a significant contributory factor in our previous observations of mesoscale molecular ordering in DPPC bilayers.[31−33] Calorimetric measurements on aged stearoylSM/cholesterol mixtures show that a second broad crystalline−gel phase transition occurs between 6 and 22 °C below T_m, and therefore supported PSM bilayers at 23 °C are also likely to be in a pseudocrystalline phase.[34] In order to verify this, we imaged PSM bilayers in PBS buffer at 23 ± 1 °C and verified the existence of crystalline lipid headgroup order (Figure S1 of the Supporting Information [SI]).

Only short-range ordering (with coherence lengths of 2.1−2.5 nm) have been observed by grazing angle X-ray diffraction of 1:1 PSM/dihydrocholesterol monolayers below T_m.[35] Additionally, phase diagrams, based on fluorescent microscopy studies of vesicles composed of PSM/cholesterol/DOPC, indicate that at 23 °C the model raft domains are in a liquid-ordered (l_o) phase and the model nonraft domains are in a liquid-disordered (l_d) phase.[36−39]

We should therefore consider the effect of the mica substrate and its interaction with the raft domains. It is well-known from neutron diffraction and reflectivity studies that an underlying water layer of 1−3 nm exists between the bilayer and supporting substrate.[26,39] Surface force apparatus studies also show that that ordered hydration layers are adsorbed to mica surfaces.[40] Previous AFM studies in this group have also shown that ordered hydration layers also adjoin supported DPPC bilayers.[19] We therefore anticipate coupling between the mica substrate and bilayer mediated by indirect hydrogen-bonding interactions between adjacent hydration layers. Electrostatic interactions between the zwitterionic lipid headgroups and cations adsorbed to the mica lattice are also likely to occur.[20]

Such interactions are likely to reduce the lateral diffusion rate of the lipid molecules forming the raft phase and therefore modify the raft phase state. Indeed, lipid lateral diffusion coefficients of supported (on oxidized silicon) fluid phase bilayers are known to be approximately 1 order of magnitude lower than free bilayers.[41] Additionally, these supported bilayers below T_m show an increase in the activation energy associated with lateral diffusion of 1 order of magnitude.[41] Such a significant change in the activation energy would reduce lateral diffusion rates by many orders of magnitude when the temperature is reduced from T_m to 23 °C. Ternary phase diagrams of PSM/cholesterol/DOPC bilayers indicate that this would shift the raft phase state from the $l_d + l_o$ phase toward the $l_d + s_o$ phase.[36−38]

In order to verify this hypothesis, we imaged mica-supported 1:1 PSM/cholesterol bilayers, which in free bilayers have been shown by previous and independent studies to be clearly in an l_o phase.[22,36,38] We found these samples to show lipid headgroup ordering over at least 10 nm (Figure S2 of the SI), verifying that interactions between the mica substrate and the bilayer induce pseudocrystalline ordering of the lipid molecules that would otherwise be in a liquid-ordered phase when free in solution. The mica-supported model raft bilayer therefore contains s_o/l_d phases rather than l_o/l_d phases. Indeed, given the time scales of image acquisition of 2−4 min/frame, it would likely not be possible to image l_o or l_d phase bilayer headgroup structure given typical lipid lateral diffusion rates of the order of micrometers per second. It should also be noted that the AFM tip scan speeds (100−600 nm/s) are such that the tip will interact with an individual headgroup over time scales of the order of milliseconds, and therefore the topography of the headgroup features imaged are time-averaged and dependent on their degree of motion.

Nanometer-Scale Imaging of Model Raft Domain Boundaries. Also from Figure 1B, it can be seen that headgroup ordering occurs in the nonraft phase confined between the two raft domains. This is likely to arise from lateral confinement induced by the surrounding ordered raft phase boundaries. The range of this induced ordering was determined from images of more isolated boundaries as approximately 10 nm, or approximately 13 lipid molecular diameters (Figure S3 of the SI). Headgroup ordering was not observed in the nonraft phase which was not in close proximity to raft domains (Figure S4 of the SI).

The highest resolution image obtained of a raft boundary is shown in Figure 2.

Both trace and retrace images (tip scanning left to right and vice versa) are shown, as a comparison between the two allows

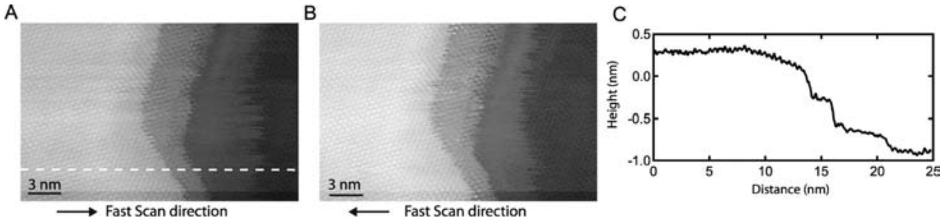

Figure 2. (A) Trace and (B) retrace high-resolution FM-AFM height images of the domain boundary of a model lipid raft imaged in PBS solution at pH 7.4 showing two intermediate steps between the raft (lightest region) and nonraft domains (darkest region). The higher (lighter) step arises from a change in lipid composition, while the lower (darker) step corresponds to an adsorbed hydration layer, tip velocity 124 nm/s, *z*-scale 2 nm (*black* to *white*), pixel width 0.5 Å. (C) Cross section of height image in (A).

additional analysis. The image shows four layers of decreasing height. At the extreme left is the raft domain, discussed previously. Figure 2 shows that, in between the raft phase (layer at the extreme left of the images) and nonraft phase (layer at the extreme right of the images), rather than there being a sharp discontinuity at the interface, two steps of intermediate height are observed. As shown in the cross section of Figure 2C, the average height of the step adjacent to the raft domain is 5.4 Å below the average raft domain height. The width of this step varies from 2 to 5 nm from the bottom to top of the scan and does not significantly vary with scan direction. In addition, we see lipid headgroup ordering, the periodicity of which does not vary significantly compared to that of the raft phase. The variation of step width and ordering confirms that the step is a sample feature rather than an artifact arising from the tip profile.

The bilayer undergoes a significant change in lipid composition when traversing the phase boundary (from a PC:SM ratio of 3:1 to 5:7 going from the nonraft to raft phase),[22] thermodynamically favoring the formation of a bilayer of intermediate composition. The step height also indicates that this intermediate bilayer, formed between the raft and nonraft phases, either has an increased level of leaflet interdigitation or lower lipid tail chain order compared to the core raft structure. This intermediate bilayer would reduce the free energy of the raft boundary that would otherwise arise from the exposure of the hydrophobic raft bilayer core to the aqueous external environment. No stable hydration layer was detected adjacent to this layer.

The average height of the step adjacent to the nonraft domain is 2.4 Å above that of the nonraft domain. This step varies in width between 4.5 and 6.4 nm in the slow scan direction (top to bottom) for the trace image and between 2.5 and 5 nm for the retrace image. Again, the variation of step width in the slow scan direction confirms that the feature is sample related rather than an artifact of the tip profile. The higher width in the trace scan suggests that this layer is loosely bound to the bilayer surface and therefore comparatively mobile during tip-scanning at this particular imaging force and scan rate. The step does not show a high degree of order compared to that of the step adjacent to the raft domain. It does show some order toward the edge adjacent to the nonraft domain and appears to be in registry with that order (the order of the nonraft phase is that induced by the raft domain, shown earlier). We therefore assign this step to a single hydration layer associated with the domain boundary and will subsequently present additional data on hydration layers at domain boundaries taken with lower imaging force.

Nanometer-Scale Imaging of Hydration Layer Structure and Organization. With the low frequency shift set points used in this study (<30 Hz equivalent to <15 pN force), the AFM tip would spontaneously jump between the surfaces of hydration layers and the surface of the bilayer, the tip−sample interaction force at both positions (Figure 3C, points (i) and (ii)) being equivalent for the *Z*-piezo feedback loop).

These jumps spontaneously arise during the scanning of an image frame and arise from thermally induced frequency shift noise and have been previously observed in FM-AFM imaging studies.[19,20] This phenomenon can be seen in the image of a raft domain in Figure 3A. The slow scan direction is right to left, and at the position indicated by the arrows in the Figure, we see spontaneous jumps between the raft surface and the hydration layer above. The height of the hydration layers is ∼3.5 Å (Figure 3B), consistent with the diameter of water molecules.[42] An ordered structure of the water molecules forming the hydration layer is observed, indicating that the bilayer headgroups have a templating effect on the hydration layer, likely mediated by both hydrogen-bonding and electrostatic interactions arising from the ordered phosphocholine dipole network.

We also used the AFM tip to probe the surface of the raft domains, normal to the bilayer plane. Figure 3C shows a typical measurement of the interaction force measured between the AFM tip and raft domains as a function of tip−sample separation. We observed oscillatory force profiles between the AFM tip and raft domain surfaces in 77 out of 90 force measurements. Two oscillatory peaks were typically observed, the peak proximal to the bilayer with a mean width of 3.2 ± 0.3 Å and the distal peak with a mean width of 3.1 ± 0.5 Å. Given the magnitudes and reproducibility of the peak widths, we attribute the peaks as corresponding to the transition of the AFM tip through the hydration layers adjacent to the bilayer surface. Oscillatory force profiles of this type have previously been measured between atomically sharp AFM tips and DPPC bilayers[19] and have also been predicted by phospholipid membrane simulation.[43] In contrast, we did not observe any oscillatory force profiles in 100 force measurements between the AFM tip and the nonraft phase (not in close proximity to domain boundaries). As the nonraft domains are in the fluid phase at room temperature, one would not expect the formation of stable hydration layers nor oscillatory force profiles.[44] The areas under the oscillatory peaks can be determined by integration of the force−distance curves and gives the energy associated with the AFM tip transition to be 0.29 ± 0.2 kT for the proximal peak and 0.05 ± 0.04 kT for the distal peak. The smaller energy associated with the distal peak, only just detectable above the thermal noise background, indicates that the water molecules of this layer are only loosely adsorbed to the proximal water layer and are therefore likely to be much less ordered. It should be noted that these energies represent the work done during the dynamic transition (at a tip approach speed 10 nm/s) of the oscillating hydrophilic AFM tip from a bulk water phase to an ordered water phase

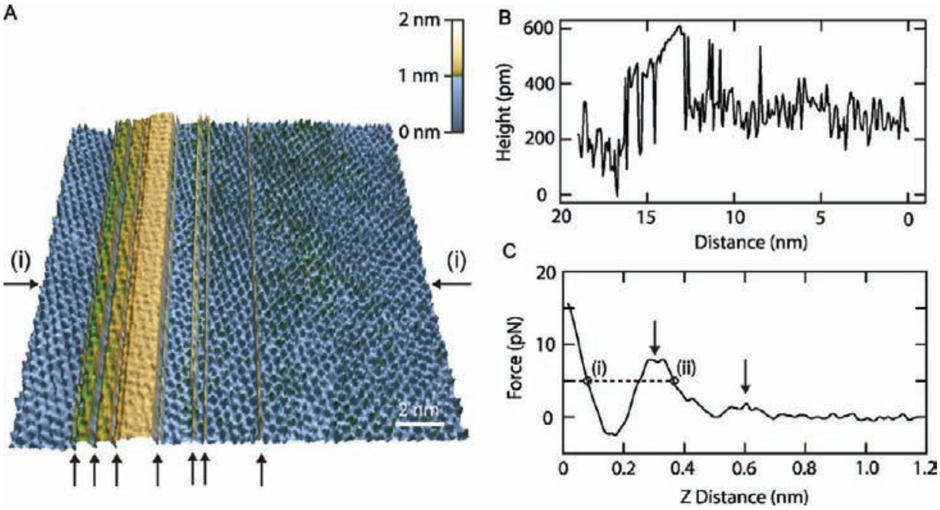

Figure 3. (A) High-resolution FM-AFM height image of the surface of a model lipid raft surface imaged in PBS solution at pH 7.4, showing the existence and structure of hydration layers adsorbed to the raft surface. The arrows indicate points on the slow scan axis (left to right of image) at which the AFM tip spontaneously jumps between the raft surface and the hydration layer above, tip velocity 196 nm/s, *z*-scale 2 nm (*black* to *white*), pixel width 0.8 Å. (B) Cross section of height image (A) along axis (i). (C) Force measured on approach of the AFM tip and raft surface as a function of tip distance above the raft surface, showing oscillatory peaks (arrowed) associated with the transition of the AFM tip through the hydration layers.

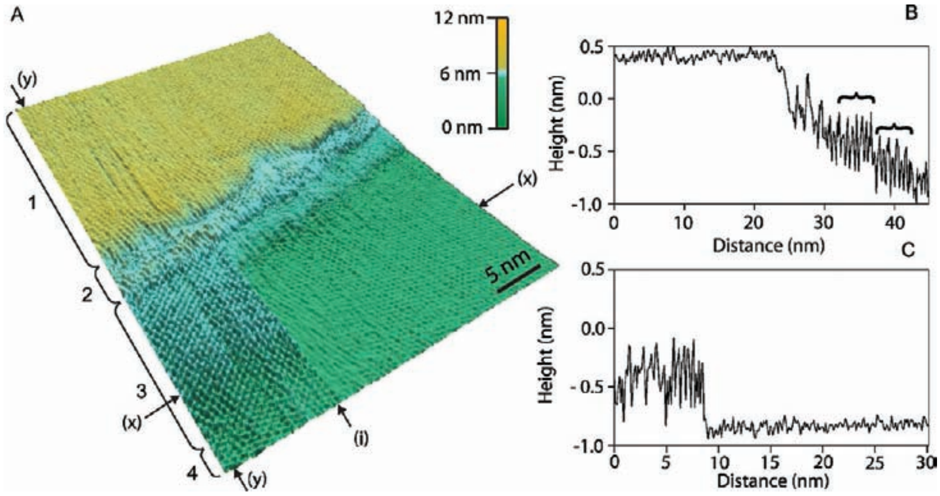

Figure 4. (A) High resolution FM-AFM height image of the domain boundary of a model lipid raft bilayer (region 1), imaged in PBS solution at pH 7.4. A bilayer of intermediate height (region 2) is seen between the raft and nonraft (regions 3 and 4) phases. Region 3 shows the structure of hydration layers (region 3) adsorbed to the ordered nonraft bilayer surface adjacent to the domain boundary. Arrow (i) indicates the point on the slow scan axis (along axis *x*, left to right) at which the AFM tip spontaneously jumped between the hydration layer and the raft surface below, tip velocity 324 nm/s, pixel width 1.3 Å. (B, C) Cross sections along axes *y* and *x*, respectively, of height image (A).

and therefore are not representative of bond energies per se. Nevertheless, the energies presented by these crystalline water layers to the atomically sharp AFM tip are finite, and therefore larger biomolecules (which may also have hydration layers associated with them) interacting with model raft domains of this type are likely to encounter significant hydration layer energy barriers.

As noted previously, we imaged hydration layers adsorbed to an ordered bilayer region surrounding the raft domains. The bilayer underneath these hydration layers is that of the nonraft phase where molecular ordering has been induced by the lateral confinement of the adjoining raft domain and as a consequence, hydration layers have formed above this region. Imaging at low frequency shift (and hence imaging force) set points allowed us to observe the structure of these hydration layers with ångstrom resolution (Figure 4A).

The higher raft domain is shown at the top of the image (region 1), and the nonraft phase is shown at the lower end of the image (regions 3 and 4). The slow scan direction is along axis *x*; at point (i), we see a spontaneous jump of the AFM tip from the nonraft bilayer surface to the hydration layer above (region 3).

From the height cross section taken along axis *y* in Figure 4B, we see that the hydration layer consists of two regions of differing heights (indicated by brackets). The first region, extending 7.6 ± 0.7 nm away from the raft boundary edge, is at a mean height of 4.0 ± 0.2 Å above that of the nonraft bilayer and has a range of 4.0 ± 0.2 Å (fwhm) which arises from the periodic height fluctuation associated with the ordered water molecules forming

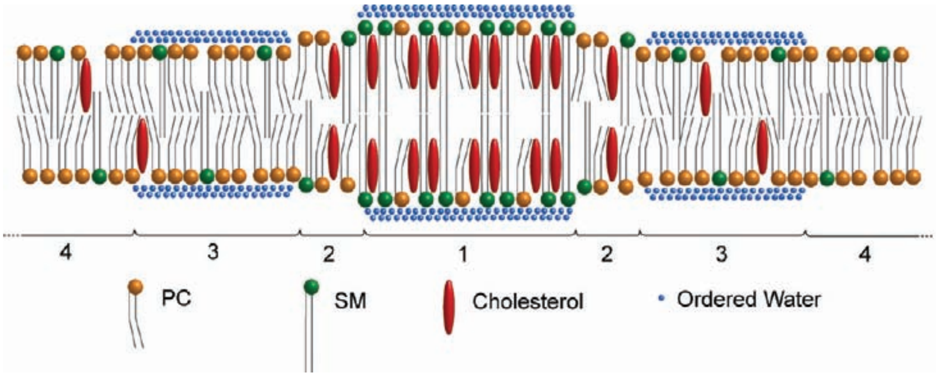

Figure 5. Schematic illustration of observed raft domain structure. Raft domains (region 1) form with mesoscale molecular order and with two crystalline hydration layers adsorbed to them. Between the raft phase (region 1) and nonraft phases (regions 3 and 4) exists a bilayer of intermediate height having a width of 2−5 nm (region 2), but without any detectable ordered hydration layers. The raft induces ordering of an annulus of width ∼10 nm around the raft domain, which in turn has two crystalline hydration layers adsorbed to it. Bulk water surrounding the bilayer has not been shown for clarity, and molecular scaling is approximate.

the hydration layer. On the basis of the diameter of a water molecule, these heights are consistent with this region of the hydration layer being formed by two layers of ordered water molecules.[42] The height of the hydration layer decays (laterally away from the raft domain boundary) over 4.0 ± 1.7 nm to the surface height of the nonraft phase, forming the second region of the hydration layer. It should be noted that the bilayer forming the nonraft phase has a height variation of 0.4 Å (fwhm). The overall range of the hydration layer away from the raft domain edge is therefore 11.6 ± 2.4 nm and is consistent with the previously observed range (10 nm) of induced ordering of the nonraft phase by the raft domains.

A schematic structure of the membrane−fluid interface for the model raft domain system studied, based on our observations, is shown in Figure 5, and we discuss the implications of the observed structure further.

Model system studies provide vital clues in deciphering more complex systems. In vivo, the plasma membrane is composed of a wide variety of different lipids of varying acyl chain lengths and saturation and at a higher temperature (∼37 °C). The phase state of in vivo raft domains will be modulated by these and many other factors, such as association with membrane proteins as well as membrane−cytoskeletal interactions. In living cells, raft domains have been shown to be small in size (∼30 nm) and raft domain diffusion rates are likely to be significantly dependent on the phase state of the nonraft phase.[8] We have observed that nonraft phase lipid molecules surround the ordered raft domains to form an annulus with a width of 10 nm. Given the relative size of the annulus compared to that of a raft domain, the effect of this annulus will be to reduce the lateral diffusion rates of the raft assembly. Another effect will be to limit the closest distance of approach of adjoining raft domains to 20 nm, which will significantly affect raft−raft interactions and also provide a physical mechanism for the maintenance of raft size by reducing the ability of rafts to coalesce into larger structures. The width of the annulus will be highly dependent on the phase composition and temperature of the nonraft phase in vivo.

We have also observed that raft domains and a 12 nm wide region around the domains have crystalline hydration layers adsorbed to them. However, the raft domain boundary of 2−5 nm width and of intermediate height and composition between the raft and nonraft phases was not observed to have stable hydration layers. This difference would suggest that raft domain boundaries would present more energetically favorable regions for interactions between rafts and external biomolecules. Indeed, studies have shown that that GPI-anchored proteins (DRMs have been shown to be rich in these proteins), such as alkaline phosphatase and ganglioside GM1, preferentially interact with model raft domain boundaries and also with the boundaries of liquid crystalline domains in phase-separated mixtures, further supporting our observations.[45,46]

The effects of hydration layers adsorbed to membranes are not generally taken into consideration in either experimental or simulation studies of membrane structure and function. In this work, we show that hydration layers have well-defined structure and organization at the membrane−fluid interface which can present significant energy barriers to interacting biomolecules.

Although raft hydration layers would not exclude other membrane-associated proteins or external biomolecules from interacting with raft-associated proteins, they would modulate the spatial location and kinetics of these interactions.

■ MATERIALS AND METHODS

Sample Preparation. Samples were prepared from synthetic single-component sphingomyelin (*N*-palmitoyl-D-erythro-sphingosylphosphorylcholine) (Avanti Polar lipids, Alabaster, AL), cholesterol (3*β*-hydroxy-5-cholestene), and DOPC (1,2-dioleoyl-*sn*-glycero-3-phosphocholine) (Sigma-Aldrich, Ireland). Stock solutions of the three components were prepared at a 5 mM concentration in a 3:1 v/v mixture of chloroform and methanol (Sigma-Aldrich, Ireland). Samples were prepared by mixing equimolar component volumes and then evaporating the solvents under an argon flow for 30 min, followed by vacuum desiccation overnight. The dried samples were rehydrated in phosphate-buffered saline (PBS) (Sigma-Aldrich, Ireland) at pH 7.4 to a total concentration of 0.5 mg/mL at a temperature of 5 °C and vortexed at 1500 rpm under argon for 5 min, with progressive heating to 55 °C. The vesicle suspension was tip-sonicated (model UPH50, Hielscher Ultrasonics GmbH, Germany) under argon for 20 min at 55 °C to generate small, unilamellar vesicles (SUVs). The samples were centrifuged at 10000 rpm for 5 min, and the supernatants were collected. Bilayers were prepared by incubation of freshly cleaved mica substrates (15 mm diameter, SPI Supplies Inc., West Chester, U.S.A.) with 100 *μ*L of SUV suspension at a temperature of 55 °C in a humidified enclosure for 1 h. Samples were rinsed by fluid exchange (10 times with 100 μL) with PBS and equilibrated for 1 h in the AFM fluid cell prior to imaging.

AFM Imaging. AM-AFM images were taken using an MFP-3D-BIO AFM (Asylum Research Inc., Santa Barbara, CA) at 26 ± 1 °C using SNL cantilevers (Veeco Instruments Ltd., U.K.) excited at a frequency of 9.3 kHz with an 11 nm free oscillation amplitude and ~0.1 nN imaging force. The optical lever sensitivities of the cantilevers were determined by force measurements against freshly cleaved mica surfaces. Spring constants were determined by the fitting of thermal oscillatory amplitude spectra with a simple harmonic oscillator model using the method of Hutter and Bechhoefer,[47] built into the software of the AFM. The imaging force was calculated from the difference between the free oscillation amplitude and the imaging amplitude set point.

FM-AFM imaging was performed at 23 ± 1 °C using a custom-built low deflection noise AFM (details of which have been previously published), driven by an MFP-3D bipolar controller (Asylum Research Inc., Santa Barbara, CA) with integrated digital FM control software using gain calculation algorithms for robust feedback tuning.[18,48] The x/y scanner was calibrated by imaging of a mica lattice in PBS buffer.

SSS-NCH-AuD silicon cantilevers (Windsor Scientific Ltd., U.K.) were used, excited in the second flexural mode at a frequency of ~900 kHz with a constant oscillation amplitude of ~2 Å. Optical lever sensitivities and spring constants were determined by the method of Higgins et al.[49]

Imaging was performed with positive frequency shifts of 5−30 Hz. As the frequency shift is proportional to the force gradient, we were imaging with the use of a short-range (<2 Å tip−sample separation, Figure 3C) repulsive tip−sample interaction.[50] In this short-range repulsive regime, Pauli repulsion forces dominate over van der Waals and electrostatic forces to produce the height contrast seen in the images.[51] The frequency shift set points corresponded to a maximum imaging force of ~15 pN. The imaging force was derived from the frequency shift set point using the algorithm by Sader and Jarvis.[52]

It should be noted that uncertainties arising from the second flexural mode shape lead to relatively high uncertainties (~75%) for absolute magnitudes of measured forces. In addition, we assume that the detected frequency shifts and subsequent calculated forces arise from interactions of the sample with the resonant mode of the cantilever. It has been shown that use of small cantilever oscillation amplitudes is an effective means of increasing lateral resolution in FM-AFM imaging due to an increase in sensitivity to short-range interaction force gradients.[53] Operation with such small oscillation amplitudes often requires the use of cantilevers with high spring constants in order to reduce the magnitude of deflection noise arising from the thermal motion of the cantilever. Previously, higher cantilever flexural modes have been employed as a practical means of accessing small-amplitude FM-AFM as a result of significant increases in the dynamic cantilever spring constants associated with these modes.[54,55] It should be noted that operating on the fundamental mode of a cantilever with stiffness equivalent to that of the flexural mode used in this study should yield the same performance.

All images were plane-fitted with a first-order polynomial function to remove the effect of sample tilt. The large scan of Figure 1A was also fitted with a second-order polynomial function in order to remove the effect of bow arising from the x/y scanner operation. The images were otherwise neither filtered nor averaged.

■ ASSOCIATED CONTENT

Ⓢ Supporting Information. Images showing Lipid order in SM and SM/cholesterol bilayers, nonraft bilayer and range of induced ordering of the nonraft phase. This material is available free of charge via the Internet at http://pubs.acs.org.

■ AUTHOR INFORMATION

Corresponding Author

khizar_001@yahoo.co.uk

■ ACKNOWLEDGMENT

We thank M. Klonowski, T. DuPar and J. Cleveland of Asylum Research Inc. for their support of low noise FM-AFM development. This work was supported by Science Foundation Ireland (07/IN.1/B931).

■ REFERENCES

(1) Simons, K.; Ikonen, E. *Nature* **1997**, *387*, 569–572.

(2) Yu, J.; Fischman, D. A.; Steck, T. L. *J. Supramol. Struct.* **1973**, *1*, 233–247.

(3) Brown, D. A.; Rose, J. K. *Cell* **1992**, *68*, 533–544.

(4) Hanada, K.; Nishijima, M.; Akamatsu, Y.; Pagano, R. E. *J. Biol. Chem.* **1995**, *270*, 6254–6260.

(5) Simons, K.; Ehehalt, R. *J. Clin. Invest.* **2002**, *110*, 597–603.

(6) Dietrich, C.; Yang, B.; Fujiwara, T.; Kusumi, A.; Jacobson, K. *Biophys. J.* **2002**, *82*, 274–284.

(7) Schutz, G. J.; Kada, G.; Pastushenko, V. P.; Schindler, H. *EMBO J.* **2000**, *19*, 892–901.

(8) Pralle, A.; Keller, P.; Florin, E.-L.; Simons, K.; Hörberet, J. K. H. *J. Cell Biol.* **2000**, *148*, 997–1008.

(9) Varma, R.; Mayor, S. *Nature* **1998**, *394*, 798–801.

(10) Ge, M.; Field, K. A.; Aneja, R.; Holowka, D.; Baird, B.; Freed, J. H. *Biophys. J.* **1999**, *77*, 925–933.

(11) Giocondi, M.-C.; Vié, V.; Lesniewska, E.; Goudonnet, J.-P.; Le Grimellec, C. *J. Struct. Biol.* **2000**, *131*, 38–43.

(12) Jacobson, K.; Mouritsen, O. G.; Anderson, R. G. W. *Nat. Cell Biol.* **2007**, *9*, 7–14.

(13) Henderson, E. *Prog. Surf. Sci.* **1994**, *46*, 39–60.

(14) Connell, S. D.; Smith, D. A. *Mol. Membr. Biol.* **2005**, *23*, 17–28.

(15) Volker, F.; Loi, S.; Muller, H.; Bamberg, E.; Butt, H.-J. *Colloids Surf., B* **2002**, *23*, 191–200.

(16) Das, C.; Sheikh, K. H.; Olmsted, P. D.; Connell, S. D. *Phys. Rev. E: Stat., Nonlinear Soft Matter Phys.* **2010**, *82*, 041920.

(17) Gross, L. *Nature Chem.* **2011**, *3*, 273–278.

(18) Fukuma, T.; Jarvis, S. P. *Rev. Sci. Instrum.* **2006**, *7*, 043701.

(19) Fukuma, T.; Higgins, M. J.; Jarvis, S. P. *Biophys. J.* **2007**, *92*, 3603–3609.

(20) Loh, S.-H.; Jarvis, S. P. *Langmuir* **2010**, *26*, 9176–9178.

(21) Sheikh, K. H.; Giordani, C.; Kilpatrick, J. I.; Jarvis, S. P. *Langmuir* **2011**, *27*, 3749–3753.

(22) de Almeida, R. F. M.; Fedorov, A.; Prieto, M. *Biophys. J.* **2003**, *85*, 2406–2416.

(23) Rinia, H. A.; Snel, M. M. E.; van der Eerden, J. P. J. M.; de Kruijff, B. *FEBS Lett.* **2001**, *501*, 92–96.

(24) Goksu, E. I.; Vanegas, J. M.; Blanchette, C. D.; Lin, W.-C.; Longo, M. L. *Biochim. Biophys. Acta* **2009**, *1788*, 254–266.

(25) Bondi, A. *J. Phys. Chem.* **1964**, *68*, 441–451.

(26) Büldt, G.; Gally, H. U.; Seelig, A.; Seelig, J.; Zaccai, G. *Nature* **1978**, *271*, 182–184.

(27) Niemalä, P.; Hyvönen, M. T.; Vattulainen, I. *Biophys. J.* **2004**, *87*, 2796–2989.

(28) Raudino, A.; Mauzerall, D. *Biophys. J.* **1986**, *50*, 441–449.

(29) Bittman, R.; Kasireddy, C. R.; Mattjus, P.; Slotte, J. P. *Biochemistry* **1994**, *33*, 11776–11781.

(30) Sun, W.-J.; Suter, R. M.; Knewtson, M. A.; Worthington, C. R.; Tristram-Nagle, S.; Zhang, R.; Nagle, J. F. *Phys. Rev. E: Stat., Nonlinear Soft Matter Phys.* **1994**, *49*, 4665–4676.

(31) Chen, S. C.; Sturtevant, J. M.; Gaffney, B. J. *Proc. Natl. Acad. Sci. U.S.A.* **1980**, *77*, 5060–5063.

(32) Ruocco, M. J.; Shipley, G. G. *Biochim. Biophys. Acta* **1982**, *684*, 59–66.

(33) Ruocco, M. J.; Shipley, G. G. *Biochim. Biophys. Acta* **1982**, *691*, 309–320.

(34) Estep, T. N.; Freire, E.; Anthony, F.; Barenholtz, Y.; Biltonen, R. L.; Thompson, T. E. *Biochemistry* **1981**, *20*, 7115–7118.

(35) Ege, C.; Ratajczak, M. K.; Majewski, J.; Kjair, K.; Lee, K. C. *Biophys. J.* **2006**, *91*, L01–L03.

(36) Veatch, S. L.; Keller, S. L. *Phys. Rev. Lett.* **2005**, *94*, 148101.

(37) Nyholm, T. K. M.; Lindroos, D.; Westerlund, B.; Slotte, J. P. *Langmuir* **2011**, *27*, 8339–8350.

(38) Marsh, D. *Biochim. Biophys. Acta* **2009**, *1788*, 2114–2123.

(39) Koenig, B. W.; Krueger, S.; Orts, W. J.; Majkrzak, C. F.; Berk, N. F.; Silverton, J. V.; Gawrisch, K. *Langmuir* **1996**, *12*, 1343–1350.

(40) Israelachvili, J. N.; Pashley, R. M. *Nature* **1983**, *306*, 249–250.

(41) Tamm, L. K.; McConnell, H. M. *Biophys. J.* **1985**, *47*, 105–113.

(42) Zhang, Y.; Xu, Z. *Am. Mineral.* **1995**, *80*, 670–675.

(43) Berkowitz, M. L.; Bostick, D. L.; Pandit, S. *Chem. Rev.* **2006**, *106*, 1527–1539.

(44) Higgins, M. J.; Polcik, M.; Fukuma, T.; Sader, J. E.; Nakayama, Y.; Jarvis, S. P. *Biophys. J.* **2006**, *91*, 2532–2542.

(45) Milhiet, P.-E.; Giocondi, M.-C.; Baghdadi, O.; Ronzon, F.; Roux, B.; Le Grimellec, C. *EMBO Rep.* **2002**, *3*, 485–490.

(46) Yokoyama, S.; Ohta, Y.; Sakai, H.; Abe, M. *Colloids Surf. B* **2004**, *34*, 65–68.

(47) Hutter, J. L.; Bechhoefer, J. *Rev. Sci. Instrum.* **1993**, *64*, 1868–1873.

(48) Kilpatrick, J. I.; Gannepalli, A.; Cleveland, J. P.; Jarvis, S. P. *Rev. Sci. Instrum.* **2009**, *80*, 023701.

(49) Higgins, M. J.; Polcik, M.; Fukuma, T.; Sader, J. E.; Nakayama, Y.; Jarvis, S. P. *Rev. Sci. Instrum.* **2006**, *77*, 013701.

(50) Albrecht, T. R.; Grütter, P.; Horne, D.; Rugar, D. *J. Appl. Phys.* **1991**, *69*, 668–673.

(51) Gross, L.; Mohn, F.; Moll, N.; Liljeroth, P.; Meyer, G. *Science* **2009**, *325*, 1110–1114.

(52) Sader, J. E.; Jarvis, S. P. *Appl. Phys. Lett.* **2004**, *84*, 1801–1803.

(53) Kawai, S.; Kitamura, S.; Kobayashi, D.; Meguro, S.; Kawakatsu, H. *Appl. Phys. Lett.* **2005**, *86*, 193107.

(54) Sugimoto, S.; Innami, S.; Abe, M.; Custance, O.; Morita, S. *Appl. Phys. Lett.* **2007**, *91*, 093120.

(55) Kawai, S.; Kawakatsu, H. *Appl. Phys. Lett.* **2006**, *88*, 133103.